NeuroImage 200 (2019) 690–703

Contents lists available at ScienceDirect

NeuroImage

journal homepage: www.elsevier.com/locate/neuroimage

Optimization of data acquisition and analysis for fiber ball imaging

Hunter G. Moss [a,b], Emilie T. McKinnon [a,b,c], G. Russell Glenn [a,b,c,d,e], Joseph A. Helpern [a,b,c,d], Jens H. Jensen [a,b,d,*]

[a] Center for Biomedical Imaging, Medical University of South Carolina, Charleston, SC, USA
[b] Department of Neuroscience, Medical University of South Carolina, Charleston, SC, USA
[c] Department of Neurology, Medical University of South Carolina, Charleston, SC, USA
[d] Department of Radiology and Radiological Science, Medical University of South Carolina, Charleston, SC, USA
[e] Department of Internal Medicine, Palmetto Health Richland Hospital, University of South Carolina School of Medicine, Columbia, SC, USA

ARTICLE INFO

Keywords:
Fiber ball imaging
Fiber orientation density function
Axon
White matter
Diffusion MRI
Funk transform

ABSTRACT

The inverse Funk transform of high angular resolution diffusion imaging (HARDI) data provides an estimate for the fiber orientation density function (fODF) in white matter (WM). Since the inverse Funk transform is a straightforward linear transformation, this technique, referred to as fiber ball imaging (FBI), offers a practical means of calculating the fODF that avoids the need for a response function or nonlinear numerical fitting. Nevertheless, the accuracy of FBI depends on both the choice of *b*-value and the number of diffusion-encoding directions used to acquire the HARDI data. To inform the design of optimal scan protocols for its implementation, FBI predictions are investigated here with *in vivo* data from healthy adult volunteers acquired at 3 T for *b*-values spanning 1000 to 10,000 s/mm^2, for diffusion-encoding directions varying in number from 30 to 256 and for TE ranging from 90 to 120 ms. Our results suggest *b*-values above 4000 s/mm^2 with at least 64 diffusion-encoding directions are adequate to achieve reasonable accuracy with FBI for calculating axon-specific diffusion measures and for performing WM fiber tractography (WMFT).

1. Introduction

A typical imaging voxel for diffusion MRI (dMRI) on a clinical scanner encompasses a volume of roughly 10–30 mm^3. In white matter (WM), a voxel of this size usually contains between several hundred thousand to several million individual axons. In some voxels, most of the axons will be oriented in similar directions, but the majority of voxels will include a broad range of orientations (Jeurissen et al., 2013). In general, the distribution of orientations is described by the fiber orientation density (or distribution) function (fODF), which gives the volume-weighted angular density of axons along a given direction.

From the fODF, it is straightforward to calculate rotationally invariant microstructural parameters, such as the fractional anisotropy axonal (FAA) (McKinnon et al., 2018), that characterize axon-specific properties of WM. More conventional diffusion measures, including the fractional anisotropy (FA) and mean diffusivity (MD), are in contrast affected by both the intra-axonal and extra-axonal tissue compartments. Additionally, the fODF plays a central role in WM fiber tractography (WMFT), where the fODFs from adjacent voxels are used as building blocks in constructing streamline representations of axonal fiber pathways (Jeurissen et al., 2019).

Several methods for estimating the fODF from dMRI data have been proposed (Anderson, 2005; Daducci et al., 2014; Schilling et al., 2018; Tournier et al., 2004, 2007; Wilkins et al., 2015). These methods typically involve nonlinear fitting to a specific signal model or assume that the signal from any fiber bundle is described by a single response function (Lazar, 2010; Tournier et al., 2011), for example, as in constrained spherical deconvolution (CSD) (Tournier et al., 2007). A recently proposed alternative method of calculating the fODF, known as fiber ball imaging (FBI), is based on the inverse Funk transform of high angular

Abbreviations: CSD, constrained spherical deconvolution; CSF, cerebrospinal fluid; DKI, diffusional kurtosis imaging; dMRI, diffusion MRI; dODF, diffusion orientation distribution function; DTI, diffusion tensor imaging; FA, fractional anisotropy; FAA, fractional anisotropy axonal; FBI, fiber ball imaging; fODF, fiber orientation density function; HARDI, high angular resolution diffusion imaging; MD, mean diffusivity; MK, mean kurtosis; NI, negativity index; SNR, signal-to-noise ratio; QBI, q-ball imaging; WM, white matter; WMFT, white matter fiber tractography.

* Corresponding author. Department of Neuroscience, Medical University of South Carolina Basic Science Building, MSC 510, 173 Ashley Avenue, Suite 403, Charleston, SC, 29425, USA.

E-mail address: jense@musc.edu (J.H. Jensen).

https://doi.org/10.1016/j.neuroimage.2019.07.005
Received 9 January 2019; Received in revised form 29 May 2019; Accepted 2 July 2019
Available online 5 July 2019

resolution diffusion imaging (HARDI) data obtained at b-values (b) equal to or greater than about 4000 s/mm^2 (Jensen et al., 2016). The inverse Funk transform (Bailey et al., 2003; Funk, 1913, 1915; Minkowski, 1904) is closely related to the inverse Radon transform, which is widely used in X-ray computed tomography (Quinto, 2006), and it corresponds to an elementary linear mapping that dispenses with both nonlinear fitting and empirically determined response functions. In this way, FBI may potentially yield more reliable predictions for the fODF.

FBI bears a strong resemblance to the q-ball imaging (QBI) approach, which employs the forward Funk transform (also known as the Funk-Radon transform) of HARDI data (Descoteaux et al., 2007; Hess et al., 2006; Tuch, 2004). An essential difference between these two methods is that QBI was devised to approximate a diffusion orientation distribution function (dODF), reflecting the directional dependence of water diffusion, rather than the angular density of fibers represented by the fODF. Furthermore, as we shall discuss, the dODF of QBI can alternatively be understood, within WM, as the result of smoothing the fODF through suppression of higher degree spherical harmonics. Thus, the dODF of QBI provides a lower fidelity representation of axonal fiber bundle orientations than does the fODF of FBI. We note that these considerations may not necessarily apply to any of several techniques (Aganj et al., 2010; Canales-Rodriguez et al., 2009; Tristán-Vega et al., 2009) that are closely related to the original QBI method (Tuch, 2004).

Although the theory underlying FBI has been presented in detail (Jensen et al., 2016) and applied in several prior works (Jensen and Helpern, 2018; Jensen et al., 2017; Li et al., 2019; McKinnon and Jensen, 2019; McKinnon et al., 2017, 2018), practical issues related to the optimization of data acquisition and analysis for FBI have not been thoroughly explored. In this paper, we first test experimentally the b-value dependence of the dMRI signal predicted by FBI. We then examine how the choice of b-value and number of diffusion-encoding directions affect the calculated fODF in order to provide recommended values for these imaging parameters. We also consider the optimization of the fODF reconstruction and the calculation of two associated microstructural parameters: the FAA and a quantity we refer to as ζ, which is proportional to the intra-axonal water fraction. Although our main focus is on the fODF and its associated microstructural parameters, we provide examples of FBI-based WMFT and compare these with conventional diffusion tensor imaging (DTI)-based, QBI-based and CSD-based WMFT.

1.1. Theory

1.1.1. The Funk transform

The Funk transform is a linear mapping of a function defined on the surface of a sphere to another function on a sphere (Bailey et al., 2003). For an arbitrary function G of a unit direction vector $\mathbf{n}$ (indicating a point on a sphere), the Funk transform is defined by

$$T_F(G,\mathbf{n}) = \int_0^{2\pi} d\phi\, G[\mathbf{m}\cos\phi + (\mathbf{m}\times\mathbf{n})\sin\phi] \tag{1}$$

where $\mathbf{m}$ is any unit vector satisfying $\mathbf{n}\cdot\mathbf{m} = 0$. Thus, the Funk transform replaces the value of G at $\mathbf{n}$ with the integral of G taken over all points orthogonal to $\mathbf{n}$. The integration paths needed to compute the Funk transform are the great circles of the sphere. For any function with antipodal symmetry [i.e., $G(-\mathbf{n}) = G(\mathbf{n})$], the Funk transform is invertible.

A practical method of computing the Funk transform and its inverse (when it exists) is based on the spherical harmonic expansion of G:

$$G(\mathbf{n}) = \sum_{l=0}^{\infty}\sum_{m=-l}^{l} \alpha_l^m Y_l^m(\theta,\phi) \tag{2}$$

where $Y_l^m(\theta,\phi)$ are the spherical harmonics, θ and ϕ are the spherical angles for $\mathbf{n}$, and α_l^m are the expansion coefficients (Funk, 1913; Hess et al., 2006; Minkowski, 1904). The expansion coefficients of odd degree l vanish when G has antipodal symmetry while the even coefficients vanish for odd reflection symmetry. In terms of spherical harmonics, the Funk transform can be written as

$$T_F(G,\mathbf{n}) = 2\pi\sum_{l=0}^{\infty} P_l(0)\sum_{m=-l}^{l}\alpha_l^m Y_l^m(\theta,\phi) \tag{3}$$

with $P_l(x)$ being the Legendre polynomial of degree l. For $x = 0$, the Legendre polynomial has the explicit expression

$$P_l(0) = \begin{cases} (-1)^{l/2}\dfrac{l!}{2^l[(l/2)!]^2}, & \text{even } l, \\ 0, & \text{odd } l. \end{cases} \tag{4}$$

Since $P_l(0)$ vanishes for odd degrees, Equation (3) is equivalent to

$$T_F(G,\mathbf{n}) = 2\pi\sum_{l=0}^{\infty} P_{2l}(0)\sum_{m=-2l}^{2l}\alpha_{2l}^m Y_{2l}^m(\theta,\phi) \tag{5}$$

From Equation (5), it is evident that the inverse Funk transform is given by

$$T_F^{-1}(G,\mathbf{n}) = \frac{1}{2\pi}\sum_{l=0}^{\infty}\frac{1}{P_{2l}(0)}\sum_{m=-2l}^{2l}\alpha_{2l}^m Y_{2l}^m(\theta,\phi) \tag{6}$$

provided G has antipodal symmetry.

1.2. Fiber ball imaging

The Funk transform was first introduced into MRI through the context of QBI (Tuch, 2004). Specifically, the Funk transform of HARDI data for a single b-value shell may be interpreted as a dODF. In contrast, the core observation of FBI is that the inverse Funk transform for high b-value, single shell HARDI data provides an estimate for the fODF (Jensen et al., 2016). The inverse exists for HARDI data because the dMRI signal generally has antipodal symmetry (Grebenkov, 2007).

Since the application of the Funk transform to the fODF of FBI yields the original HARDI data, the dODF of QBI is equal to the double Funk transform of the fODF. Interestingly, a double Funk transform corresponds to a low pass filter for the spherical harmonics. To see this, note that Equation (5) implies that the double Funk transform may be expressed as

$$T_F[T_F(G,\mathbf{n}),\mathbf{n}] = (2\pi)^2\sum_{l=0}^{\infty}[P_{2l}(0)]^2\sum_{m=-2l}^{2l}\alpha_{2l}^m Y_{2l}^m(\theta,\phi) \tag{7}$$

From the approximation (Jensen et al., 2016)

$$[P_{2l}(0)]^2 \approx \frac{1}{\pi l}, \tag{8}$$

it then follows that the double Funk transform reduces the contribution of the higher degree spherical harmonics by a factor that grows roughly linearly with l. Hence, fODFs predicted from FBI will always appear sharper than dODFs of QBI generated from the same data.

Three principal assumptions underlying FBI are 1) that axons can be idealized as thin, straight cylindrical tubes, 2) that water exchange between the intra-axonal and extra-axonal spaces is small on time scales comparable to the diffusion time for the dMRI pulse sequence, and 3) the echo time is sufficiently long so that the dMRI signal from myelin water can be neglected (Jensen et al., 2016). A strong test for the validity of these assumptions is the behavior of the direction-averaged dMRI signal for large b-values. If they hold, the direction-averaged signal is expected to decrease asymptotically as $b^{-1/2}$, which has indeed been observed throughout the white matter of healthy volunteers (McKinnon et al.,

2017; Novikov et al., 2018a; Veraart et al., 2019). An additional means of testing these assumptions is to examine the b-value dependence for the power of the higher degree ($l > 0$) spherical harmonics as is discussed further below.

FBI requires the use of large b-values for two reasons (Jensen et al., 2016). First, the diffusion weighting should be strong enough so that the signal from the more mobile pool of extra-axonal water can be neglected relative to that from water confined within axons. Second, the b-value should be large in comparison to ${D_a}^{-1}$, where D_a is the intrinsic intra-axonal diffusivity, with the inverse Funk transform approaching the exact fODF in the limit $bD_a \to \infty$.

A correction to the fODF can be found by instead using a "generalized" Funk transform defined as (Jensen et al., 2016)

$$\tilde{T}_F(G,\mathbf{n}) = 2\pi \sum_{l=0}^{\infty} g_{2l}(bD_0) P_{2l}(0) \sum_{m=-2l}^{2l} \alpha_{2l}^m Y_{2l}^m(\theta,\phi) \tag{9}$$

along with the corresponding inverse

$$\tilde{T}_F^{-1}(G,\mathbf{n}) = \frac{1}{2\pi} \sum_{l=0}^{\infty} \frac{1}{g_{2l}(bD_0) P_{2l}(0)} \sum_{m=-2l}^{2l} \alpha_{2l}^m Y_{2l}^m(\theta,\phi) \tag{10}$$

As with Equation (6), Equation (10) assumes that G has antipodal symmetry. The parameter D_0 should obey $D_0 \geq D_a$ and

$$g_{2l}(x) \approx \exp\left[-\frac{l(2l+1)}{2x}\right] \tag{11}$$

with an exact formula for $g_{2l}(x)$ being given by Jensen and coworkers (Jensen et al., 2016) in terms of confluent hypergeometric functions. Both the approximate and exact expressions have the limit $g_{2l}(x) \to 1$ as $x \to \infty$, so the generalized Funk transform reduces to the conventional Funk transform as $D_0 \to \infty$ for a fixed b-value.

In our prior work (Jensen et al., 2016), we have argued that reducing D_0 for the generalized inverse Funk transform of HARDI data (without violating the constraint $D_0 \geq D_a$) should increase the accuracy of the estimated fODF at the price of amplifying the signal noise. A reasonable choice for D_0 is then $3.0\,\mu m^2/ms$, which is the diffusivity of free water at body temperature (Holz et al., 2000) and presumably an upper bound for water confined within axons. In this study, we compare corrected fODFs obtained from the generalized inverse Funk transform with $D_0 = 3.0\,\mu m^2/ms$ to the uncorrected fODF obtained from the conventional inverse Funk transform, which formally corresponds to $D_0 = \infty$. The differences between the corrected and uncorrected fODFs should diminish as the b-value for the HARDI data is increased.

1.3. Microstructural parameters

In addition to the fODF, there are two primary microstructural parameters associated with FBI, which can be estimated from the same HARDI data. The first is

$$\zeta \equiv \frac{f}{\sqrt{D_a}} \approx 2\sqrt{\frac{b}{\pi}}\,\frac{\bar{S}}{S_0} \tag{12}$$

where f is the intra-axonal water fraction, $\bar{S}$ is the direction-averaged dMRI signal, and S_0 is the signal without diffusion-weighting (Jensen et al., 2016). In Equation (12), the approximation in terms of signal intensities is valid only when the b-value is large enough for the aforementioned $b^{-1/2}$ scaling to hold. The second is the FAA, which corresponds to the FA of the fODF and is derived from the more restricted intra-axonal water compartment with the full collection of axons inside a voxel being taken as a whole (McKinnon et al., 2018). Expressing the fODF in terms of a spherical harmonic expansion

$$F(\mathbf{n}) = \sum_{l=0}^{\infty} \sum_{m=-2l}^{2l} c_{2l}^m Y_{2l}^m(\theta,\phi), \tag{13}$$

where c_{2l}^m are the expansion coefficients, allows the computation of the FAA from the analytic expression

$$\mathrm{FAA} = \sqrt{\frac{3\sum_{m=-2}^{2} |c_2^m|^2}{5|c_0^0|^2 + 2\sum_{m=-2}^{2} |c_2^m|^2}} \tag{14}$$

The FAA is a direct measure of diffusion anisotropy for water contained within axons that excludes the effects of extra-axonal water. It is guaranteed to be in the range from 0 to 1, provided the fODF is nonnegative in all directions. This is, of course, true for an exact fODF, but not necessarily true for estimated fODFs due to, for example, signal noise and imaging artifacts. If the exact fODF has sufficiently sharp features, truncating the spherical harmonic expansion of Equation (13) can result in Gibbs phenomenon ringing that might also contribute to negative fODF values (Gelb, 1997). As an axon-specific measure of diffusion anisotropy, the FAA may be helpful for elucidating whether microstructural changes in WM associated with disease or development reflect alterations of axons or of the extra-axonal space (assuming the main tenets of FBI hold in these situations).

1.4. Harmonic power

The harmonic power of the lth degree for the dMRI signal may be defined as

$$p_l \equiv \frac{1}{2l+1} \sum_{m=-l}^{l} |a_l^m|^2 \tag{15}$$

where a_l^m are the spherical harmonic expansion coefficients for the signal (Śliwa et al., 2001). The theory underlying FBI makes predictions for the b-value dependence of this power for even degrees, while the power for odd degrees generally vanishes due to the antipodal symmetry of the signal. More specifically,

$$p_l \approx \frac{u_l}{b}[g_l(bD_a)]^2 \tag{16}$$

for even degrees and large b-values, where u_l is a constant independent of b.

The harmonic power for $l = 0$ is proportional to the square of the direction-averaged signal, and the b-value dependence dictated by Equation (16) is essentially equivalent to the decrease of the signal as $b^{-1/2}$ for large b-values discussed above. However, for positive even degree harmonics, Equation (16) gives new predictions, which may be tested experimentally to further validate the FBI approach and help establish an appropriate range of b-values for its application.

2. Methods

2.1. Subjects

Six healthy adult volunteers (26–33 yrs) were recruited, but one volunteer was excluded from the analysis due to excessive motion artifacts in the MRI data. Consent was obtained for all subjects under a protocol approved by the institutional review board of the Medical University of South Carolina. Due to ethical considerations, the data used for this study cannot be made openly available.

2.2. Imaging

All imaging data were acquired on a Siemens 3T Prisma^{fit} MRI

scanner (Siemens Healthineers, Erlangen, Germany) using a 32-channel head coil. For all subjects, dMRI data were obtained using a twice-refocused echo planar imaging pulse sequence to suppress eddy current distortion (Reese et al., 2003) with a field of view of $222 \times 222\,mm^2$ and an acquisition matrix of 74×74 yielding an in-plane resolution of $3.0 \times 3.0\,mm^2$. Image volumes contained 42 contiguous axial slices with 3.0 mm slice thickness. The image acquisition utilized the "adaptive combine" coil data combination mode together with full Fourier k-space coverage, an in-plane parallel imaging factor of 2, a multiband acceleration factor of 2, and a bandwidth of 1648 Hz/px.

For three of the subjects (Subjects 1–3), HARDI data were collected using 128 diffusion-encoding directions at b-values of 1000, 2000, 4000, 6000, 8000 and 10,000 s/mm^2. For each b-value, a matching set of 11 images with the b-value set to zero (b0 images) were also acquired. The TE was 110 ms and the TR was 5300 ms resulting in an image acquisition time of about 12 min 34 s per b-value (including b0 images). For one subject (Subject 4), HARDI data were collected using a b-value of 6000 s/mm^2 with 30, 64, 128, and 256 diffusion-encoding directions and with 11 matching b0s for each set of diffusion-encoding directions. The TE was 95 ms, the TR was 5100 ms, and the total acquisition for all four HARDI datasets was approximately 45 min. For another subject (Subject 5), HARDI data were collected using a b-value of 4000 s/mm^2 with 128 diffusion-encoding directions for TE = 90, 100, 110, and 120 ms. The TR was 3900 ms, and 11 matching b0s were acquired for each TE. The total scan time for the HARDI datasets of Subject 5 was about 37 min. With TE = 90 ms, dMRI data for Subject 5 were also obtained with 30 diffusion directions and b-values of 1000 and 2000 s/mm^2. The scan time for this extra dMRI sequence was 5 min 42 s. For anatomical reference, all subjects also received a T1-weighted (MPRAGE) scan, with a TE of 2.26 ms, a TR of 2300 ms, an inversion time of 900 ms, 1 mm^3 isotropic voxels, and 192 slices.

2.3. Image processing

For each subject, the raw diffusion weighted images were denoised with a principal component analysis approach (Veraart et al., 2016), the method of moments (Gudbjartsson and Patz, 1995) was utilized to reduce Rician noise bias, and a Gibbs ringing correction (Kellner et al., 2016) was applied. Lastly, a rigid-body transformation was used to co-register the images together across b-values. The mean signal-to-noise ratio (SNR) values, for Subjects 1–3, in WM averaged across subjects were 37 ± 8, 24 ± 5, 14 ± 3, 11 ± 2, 9 ± 2 and 7 ± 1 for the b-values of 1000, 2000, 4000, 6000, 8000 and 10,000 s/mm^2, respectively. For Subject 4, mean SNR values in the WM at a b-value of 6000 s/mm^2 were 7 ± 4, 8 ± 5, 10 ± 7 and 8 ± 4 when the number of diffusion-encoding directions was 30, 64, 128 and 256, respectively. For Subject 5, mean SNR values in WM at a b-value of 4000 s/mm^2 were 9 ± 5, 9 ± 4, 8 ± 4 and 7 ± 3 for TE equal to 90, 100, 110 and 120 ms, respectively.

The spherical harmonic coefficients for the dMRI signal from each HARDI b-value shell were determined on a voxel-wise basis using linear least-squares fitting (Descoteaux et al., 2007; Hess et al., 2006). Our calculations used spherical harmonic coefficients up to and including $l = 6$ unless otherwise indicated, but we also examined the effect of truncating the expansion at either $l = 4$ or $l = 8$ for some quantities. Increasing the maximum degree of the spherical harmonic expansion improves accuracy but possibly at a price of reduced precision since the relative effect of signal noise tends to be large for higher degree harmonics (Jensen et al., 2016). Parametric maps of ζ were then determined from Equation (12), the b0 images, and the $l = 0$ spherical harmonic coefficients, which are proportional to $\bar{S}$.

The fODFs in all WM voxels were found by applying to the HARDI data for each b-value either the conventional inverse Funk transform of Equation (6) or the generalized inverse Funk transform of Equation (10). The former is referred to as the "uncorrected fODF" and the latter as the "corrected fODF". The corrected fODF is regarded as the default choice, and it was utilized in our calculations unless otherwise indicated. However, some comparisons with the uncorrected fODF were made in order to demonstrate differences between the two variants. Parametric maps for the FAA were calculated from the fODFs by using Equation (14). For comparison, using the same HARDI datasets, QBI dODFs were calculated via application of the forward Funk transform of Equation (3) and CSD fODFs were estimated via a response function using the 'fa' algorithm in MRTrix3 (http://www.mrtrix.org/). Both QBI and CSD were performed with $l_{max} = 6$.

The local maxima (peaks) for the fODFs of each voxel were determined by using the peak detection algorithm described by Glenn and coworkers (Glenn et al., 2015). The direction of the peak with the largest amplitude was taken as the principal fODF direction. Two peak filtering thresholds were tested: 10% and 40% of the largest peak amplitude. Peaks with an amplitude of less than the prescribed threshold were excluded from our analysis of fODF peak direction characteristics. The 10% threshold was selected for peak filtering as it is the default under the widely used CSD framework (Tournier et al., 2007). The 40% threshold was chosen so that the fractions of WM voxels with one, two, and three or more peaks were roughly similar to the values reported by Jeurissen and coworkers (Jeurissen et al., 2013). Small spurious peaks due to signal noise are common features of experimentally measured fODFs, and similar peak thresholds are often employed to filter these out (Wilkins et al., 2015). The analysis of peak characteristics included the variation with b-value of the principal fODF direction and of the number of detected peaks per voxel.

In order to assess the extent to which the estimated fODFs contain unphysical negative values, a negativity index (NI) was defined as

$$\mathrm{NI} \equiv \frac{\int |F(\mathbf{u})| d\Omega_{\mathbf{u}}}{\int F(\mathbf{u}) d\Omega_{\mathbf{u}}} - 1 \tag{17}$$

with the integrals being taken over all directions $\mathbf{u}$. This is zero if the fODF is positive in every direction, as should be true for the exact fODF, and increases as the fODF takes on more negative values. Negative values may result from approximations inherent in using either Equation (6) or Equation (10) to determine the fODF, from signal noise, and from imaging artifacts. However, it should be noted that both of these equations guarantee that $\int F(\mathbf{u}) d\Omega_{\mathbf{u}} > 0$ for all voxels with a nonzero signal in at least one diffusion encoding direction.

For Subjects 1–3, a diffusional kurtosis imaging (DKI) (Jensen and Helpern, 2010; Jensen et al., 2005) analysis was also performed using the dMRI data obtained with b-values of 0, 1000 and 2000 s/mm^2. Diffusional Kurtosis Estimator (DKE) (http://www.nitrc.org/projects/dke/) was applied to this data in order to obtain the diffusion and kurtosis tensors along with several standard rotationally invariant diffusion measures, such as FA, MD, and mean kurtosis (MK) (Tabesh et al., 2011).

In the analysis of the data from Subjects 1–3, a WM matter mask was defined as all voxels satisfying the conditions MD < 1.5 μm^2/ms and MK > 1 (Yang et al., 2013). Since low b-value data were not obtained for Subject 4, a DKI analysis was not possible, and therefore we instead defined a WM mask with the condition $\zeta > 0.2\,\mathrm{ms}^{1/2}/\mu\mathrm{m}$, which included mainly WM voxels as verified by reference to the anatomical T1-weighted images. In generating this second mask, we used the HARDI dataset with 256 directions. As the microstructure of cerebellar WM differs significantly from that of cerebral WM (Bush and Allman, 2003), the cerebellum was excluded from all WM masks.

For Subject 3, whole-brain deterministic WMFT was performed using the Euler method (Jeurissen et al., 2019) with the directions in each voxel being determined from up to three fODF peaks provided their amplitudes satisfied the 40% threshold condition described above. If more than three peaks satisfied the threshold, then only the three peaks with the largest amplitudes were chosen. A total of 250,000 seed points were distributed randomly throughout the WM mask, and tracks were calculated with a step size of 0.1 mm and a minimum track length of 30 mm. Tracks were terminated whenever the FA dropped below 0.1 or

the angular change in direction was greater than 35°.

For comparison, WMFT was also generated using peak directions derived from DTI, QBI, and CSD. For DTI, each voxel had a single direction corresponding to the principal diffusion tensor eigenvector. For QBI and CSD, the directions were determined in precisely the same way as for FBI, except with the dODF replacing the fODF in QBI. Identical seed points and termination criterion were employed for all four types of WMFT. Thus, any discrepancies in the WMFT generated across these approaches are attributable solely to differences in the number of peaks and their directions.

2.4. Noise simulations

In order to systematically characterize the effect of noise on the FBI results, specifically the microstructural parameters (ζ and FAA) and the estimated fODF, a series of numerical simulations were performed. The previously processed HARDI data (see *Image Processing*, first paragraph) were taken as our ground truth to which we added Rician noise, denoised again and then ran through the analysis pipeline. To generate the Rician distribution, the noise map output from the initial denoising step was employed. Each voxel value within this map corresponds to the standard deviation of the noise distribution. Consequently, this also set the simulation SNR levels to match those of the original analyses. A total of 100 numerical simulations were performed across each b-value (Subjects 1–3) and across each TE (Subject 5) with $l_{\max} = 6$. The standard deviations for the estimates of ζ, FAA and the principal fODF direction due to noise were then assessed within the WM across the simulations.

All of the computer code used for our data analysis is either in the public domain or available upon direct request.

3. Results

The direction-averaged dMRI signal, $\overline{S}$, in WM as a function of b-value is shown in Fig. 1 for Subjects 1–3. For b-values of about 4000 s/mm^2 and above, the signal decays approximately as $b^{-1/2}$ as predicted by FBI and as observed in prior studies (McKinnon et al., 2017; Novikov et al., 2018; Veraart et al., 2019). For b-values below 4000 s/mm^2, S decays more quickly than $b^{-1/2}$ due to contributions from extra-axonal water. In WM for the same three subjects, the average harmonic powers of Equation (15) with degrees $l = 2$, 4, and 6 are plotted in Fig. 2 as functions of b-value, along with two types of fits to the data based on the theoretical predictions of Equation (16). The solid lines are global fits to the full dataset with a single fitted value for D_a across degrees for each subject, while the dashed lines are fits restricted to the data for $b \geq 4000$ s/mm^2 with D_a set to 2.25 μm^2/ms. The restricted fitting is included since the data points with $b < 4000$ s/mm^2 are more prone to contamination from extra-axonal water signal, which is not accounted for in Equation (16). The value of $D_a = 2.25$ μm^2/ms is taken from Dhital and coworkers (Dhital et al., 2019). The global fits have just four adjustable parameters (D_a, u_2, u_4, and u_6) for the full dataset from each subject. For the restricted fitting, the only adjustable parameters are the three scales u_2, u_4, and u_6. The global fits match the data well, but the estimated values of D_a for the three subjects (2.94 ± 0.10, 3.15 ± 0.13, and 3.20 ± 0.12 μm^2/ms) are somewhat high in comparison to estimates of D_a obtained through alternative means (Dhital et al., 2019; Kaden et al., 2016; McKinnon et al., 2018; Novikov et al., 2018; Veraart et al., 2018a, 2019), which likely reflects a bias from the extra-axonal water. The majority of the data points are also close to the restricted fits with the more realistic D_a value, except for p_2 at $b = 1000$ and 2000 s/mm^2.

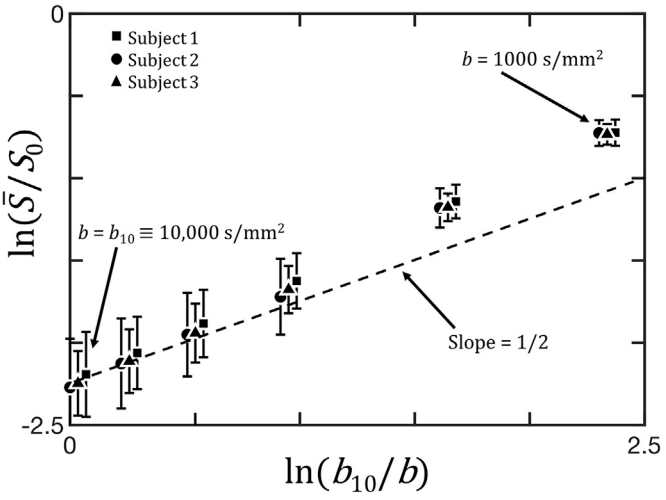

Fig. 1. Logarithm of the mean ratio between the direction-averaged dMRI signal ($\overline{S}$) and the signal without diffusion weighting (S_0) over all WM voxels from three subjects as a function of the logarithm of the ratio between a chosen reference b-value ($b_{10} \equiv 10,000$ s/mm^2) and the b-value (b) used to acquire the HARDI data. The leftmost data points correspond to $b = b_{10}$ while the rightmost data points correspond to $b = 1000$ s/mm^2. The theory underlying FBI predicts that the direction-averaged signal obeys a simple power law scaling of the form $\overline{S} \propto b^{-1/2}$, for large b-values. Thus, the data points should approach a line having a slope of one-half as the b-value is increased as is apparent for $b \geq 4000$ s/mm^2 (four leftmost b-values). Some of the subject data points have been slightly displaced in the horizontal direction to improve readability, and the error bars indicate standard deviations.

Representative parametric maps of ζ, FAA, and color FAA are shown in Fig. 3 for a single anatomical slice from one subject as calculated with $b = 1000$, 2000, 4000, 6000, 8000, and 10,000 s/mm^2. The dependence of these maps on b-value is negligible above the suggested threshold for FBI of $b = 4000$ s/mm^2. However, the maps differ noticeably below this threshold, reflecting the incomplete suppression of the extra-axonal water signal. Mean WM values for ζ and FAA from Subjects 1–3 are plotted in Fig. 4 as a function of b-value. Again, there is little b-value dependence above $b = 4000$ s/mm^2. The voxel-wise standard deviations for ζ and FAA (σ_ζ and σ_{FAA}) are plotted in Fig. 5 as functions of b-value for Subjects 1–3. Relatively stable behavior is observed for ζ even into the low SNR regime of the higher b-values. In contrast, FAA has a markedly larger spread as b-value is increased.

The effect of varying the number of diffusion-encoding directions with the b-value fixed at 6000 s/mm^2 is demonstrated in Fig. 6 for both ζ and FAA. Similar results are obtained for 64, 128, and 256 directions, but with only 30 directions lower values are seen for the mean ζ and FAA. This suggests that 64 or more directions are adequate for estimation of these two parameters, which is consistent with previously reported conclusions based on numerical simulations (McKinnon et al., 2018). The TE dependence of ζ and FAA is shown in Fig. 7 at a fixed b-value of 4000 s/mm^2 with 128 diffusion-encoding directions. For both metrics, there is no observable dependence on TE. In Fig. 8, the simulations across TE values show a slight upward trend in σ_ζ and σ_{FAA} as TE is increased from 90 to 120 ms.

Examples of both uncorrected and corrected fODFs, as calculated with FBI, are displayed in Fig. 9 for three different WM voxels from a single subject. The data were acquired with a b-value of 6000 s/mm^2 and 128 diffusion-encoding directions while the voxels were selected to represent regions with one, two, and three major peak directions. The differences between the uncorrected and corrected fODFs are subtle, but the peaks are slightly sharper for the corrected fODF. In addition to the major peaks, several smaller peaks are apparent, which could be due to noise and/or represent true fine structure of the fODF. Such smaller peaks would typically not be employed in WMFT. Also shown in Fig. 9 are the diffusion ellipsoid of DTI, the dODF of QBI, and the fODF of CSD for the same three voxels. The diffusion ellipsoids were calculated using HARDI data for $b = 1000$ s/mm^2, and the same data as for the FBI fODFs were used to generate the QBI dODFs and CSD fODFs. The diffusion ellipsoid always has a single peak direction corresponding to the principal

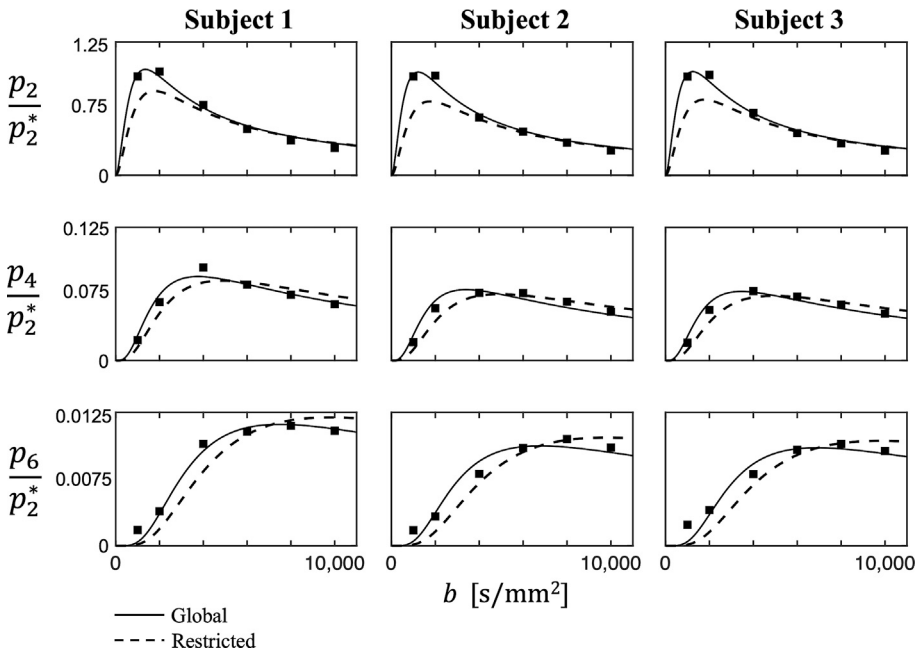

Fig. 2. Measured harmonic power (p_l) for $l = 2$, 4, and 6 as a function of b-value, normalized by the power for $l = 2$ at $b = 1000$ s/mm^2 (p_2^*), together with theoretical fits based on Equation (16). Each data point represents a mean for the WM voxels of an individual subject. The solid lines are global fits using the full dataset, while the dashed lines are restricted fits for just the data points with $b \geq 4000$ s/mm^2. The global fits treat the intra-axonal diffusivity, D_a, as an adjustable parameter for each subject, whereas the restricted fits assume a literature value of $D_a = 2.25$ μm^2/ms (Dhital et al., 2019). Thus, the full set of data for each subject was fit with only four adjustable parameters for the global fits and three adjustable parameters for the restricted fits. The theoretical predications are in reasonable accord with the experimental measurements, except for the restricted fits to some of the data points with $b < 4000$ s/mm^{2}particularly for $l = 2$. These discrepancies may be due to contributions to the dMRI signal from extra-axonal water, which are not included in Equation (16). Error bars are omitted since the standard errors of the mean are small in comparison to the size of the data symbols.

diffusion tensor eigenvector excluding exceptional cases in which the diffusion tensor has degenerate eigenvalues. As a consequence, DTI-based WMFT utilizes only one direction in each voxel and is not able to faithfully represent voxels with fiber crossings (Lazar, 2010). The QBI dODF, in contrast, is able to resolve fiber crossings by detecting multiple peak directions per voxel. However, the peaks for the dODFs are not as pronounced as those for the fODFs reflecting the fact that the dODF is the result of smoothing the uncorrected FBI fODF with a double Funk transform. This blurred nature of the QBI dODF may impact both the accuracy and sensitivity of QBI-based WMFT. The CSD fODFs are comparable to the FBI fODFs in sharpness and multiple direction characteristics. There are more tiny (potentially spurious) peaks visible near the centers of the CSD fODFs compared to the FBI fODFs.

The estimated dODF/fODF shapes across b-values are shown in Fig. 10 for QBI, CSD and FBI in the same three voxels as in Fig. 9. The uncorrected and corrected FBI fODFs both become sharper as the b-value is increased, with the corrected fODF maintaining its shape better at low b-values. The uncorrected and corrected FBI fODFs begin to converge to similar glyph shapes between approximately $b = 4000$ and 6000 s/mm^2. The CSD fODF shows consistency across b-values for all three fiber cases and has similar features as the corrected FBI fODF. For the QBI dODF, multiple directions only become clearly discernible for $b = 4000$ s/mm^2 and above in the two and three fiber cases.

To assess the effect of employing the generalized Funk transform of Equation (10), the mean FAA differences (ΔFAA) as calculated using the corrected and uncorrected fODFs are plotted in Fig. 11 as a function of b-value for Subjects 1–3. The corrected fODF always has a larger FAA than the uncorrected fODF, which is consistent with the notion of the corrected fODF being sharper. However, as b is increased, the FAA differences decrease reflecting the convergence of the standard and generalized Funk transforms for large b-values.

The fractions of WM voxels from Subjects 1–3 with one, two, and three or more detected peak directions per voxel as a function of the b-value are plotted in Fig. 12. All directions were obtained from the corrected fODF with the peak threshold set at either 10% or 40% of the largest peak amplitude. When a peak filtering threshold of 10% is applied, the voxel fractions of one and two peak directions are low, with most voxels being identified as having three or more peaks. When filtering peaks using the 40% threshold, for b-values of 4000 s/mm^2 and above, the voxel fractions are fairly consistent with each other; for lower b-values, the fraction of voxels with one or two peaks decreases sharply, while the fraction with three or more increases correspondingly. This suggests that FBI-based WMFT should employ b-values of at least 4000 s/mm^2.

Fig. 13 plots the absolute angular difference (θ) between the principal (corrected) fODF peak direction at a given b-value and the principal fODF direction at $b = 10{,}000$ s/mm^2 with $l_{max} = 4$, 6 and 8 for Subjects 1–3. The data points are averages over all WM voxels. By definition, the data points at $b = 10{,}000$ s/mm^2 are precisely zero. For all b-values at $l_{max} = 4$, the mean angular differences are all close to 5°. For $b = 2000$, 4000, 6000, and 8000 s/mm^2 at $l_{max} = 6$, the mean angular differences are also close to 5°, while they exceed 10° for $b = 1000$ s/mm^2. Similar observations are made at $l_{max} = 8$, except that the mean angular differences at $b = 2000$ s/mm^2 now exceed 10°. That these differences are amplified at $l_{max} = 8$ and may reflect the effects of signal noise. Fig. 14 shows the absolute angular differences, again averaged in the WM, between the principal peak directions for the uncorrected and corrected fODFs at $l_{max} = 4$, 6 and 8 using the same data as for Fig. 13. For all l_{max} values, the mean differences decrease with increasing b-value to less than approximately 2° for $b = 10{,}000$ s/mm^2. The noise simulation results in Fig. 15 show that for 4000 s/mm^2 $\leq b \leq$ 8000 s/mm^2 the voxel-wise standard deviations of the angular difference of the principal fODF peak direction (σ_θ) are similar.

In Fig. 16, mean angular differences in the WM of Subject 4 across the number of diffusion-encoding directions are shown for $l_{max} =$ 4, 6 and 8. It is seen that differences of the fODF principal direction (referenced to 256 directions, for which the difference is zero by definition) have similar values for 64 and 128 directions. There is a substantial increase in the angular differences going from $l_{max} =$ 4 to $l_{max} =$ 8 at 30 encoding directions.

The mean angular difference across TE values within the WM of Subject 5 for $l_{max} = 4$, 6 and 8 are plotted in Fig. 17. Similar values are observed across all TE's where the differences for TE = 90 ms are zero by definition. Simulation results for voxel-wise standard deviations in the WM of Subject 5 across TE's are provided in Fig. 18 where stable behavior is observed across all TE's. Again, the point for TE = 90 ms is zero by definition.

The NI, as defined by Equation (17), is plotted as a function of b-value in Fig. 19 for $l_{max} = 4$, 6 and 8. The data points are mean WM values for Subjects 1–3. The NI is less than 0.1 for all data points with

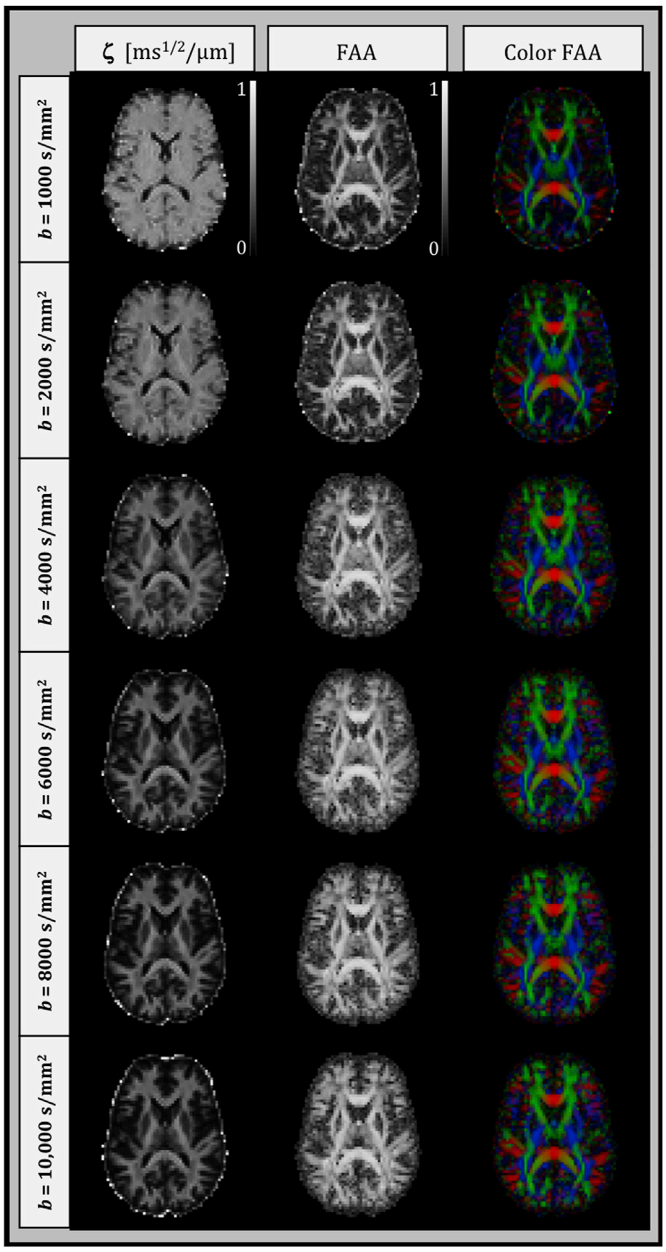

Fig. 3. Parametric maps of FBI-derived measures from one subject for a single anatomical slice. The columns, from left to right, show ζ, FAA, and color FAA maps for b-values ranging from 1000 to 10,000 s/mm^2. The calibration bar for ζ has units of ms$^{1/2}$/μm while FAA is dimensionless. The color FAA depicts directionality where the convention is left-right (red), anterior-posterior (green), and superior-inferior (blue). FBI predictions are only meaningful in WM regions and are expected to become more accurate with increasing b-value as the contributions from extra-axonal water are further reduced.

$b \geq 2000$ s/mm^2 at $l = 4$ and 6 indicating that the fODFs take on primarily positive values. For $l = 8$, the corrected fODF has large NI values (not shown) for $b \leq 2000$ s/mm^2, but for $b \geq 4000$ s/mm^2 these values are only slightly larger than those with $l = 4$ and 6. The NI for the corrected fODF across all degrees is substantially larger than for the uncorrected fODF, which may be due, in part, to a greater sensitivity to signal noise for the generalized inverse Funk transform than for the conventional inverse Funk transform (Jensen et al., 2016).

Whole-brain WMFT for Subject 3 is shown in Fig. 20 as calculated using the peak directions obtained from DTI, QBI, CSD and FBI. For FBI, examples for both the uncorrected and corrected fODFs are given. The DTI-based WMFT used the HARDI data with $b = 1000$ s/mm^2 while the WMFT for QBI, CSD and FBI employed the same data with $b = 6000$ s/mm^2. Of the four cases, the DTI-based WMFT is the sparsest reflecting the fact that DTI provides only a single direction per voxel. The FBI-based WMFT is noticeably more extensive than the QBI-based WMFT possibly due to FBI's higher sensitivity to fiber crossings. FBI-based WMFT using the uncorrected fODF is similar to that obtained with the corrected fODF. The CSD-based WMFT closely resembles the FBI-based WMFT.

4. Discussion

A central premise of FBI is that the spherical harmonic expansion coefficients of HARDI data for strong diffusion weightings are dominated, in WM, by the contributions from intra-axonal water (Jensen et al., 2016). As a consequence, in applying FBI, it is crucial to employ a sufficiently large b-value in order to adequately suppress the effects of extra-axonal water. In prior work, an appropriate b-value threshold was estimated by examining how the direction-averaged HARDI data and the microstructural parameter ζ depend on diffusion weighting (McKinnon et al., 2017). Here, we have extended this previous analysis by also investigating the b-value dependence of higher harmonic powers for the HARDI data, of the FAA, and of the fODF peak directions. Our results confirm prior results that a minimum b-value of about 4000 s/mm^2 is sufficient, at 3 T, for the b-value dependence of the direction-averaged dMRI signal to follow the predictions of FBI. There is also good consistency between theory and experiment for the $l = 2$, 4, and 6 harmonic powers providing a significant additional validation of the FBI approach as well as for the "stick" model of WM in general (Novikov et al., 2018a). Our observation that FBI predictions for FAA and fODF peak directions are relatively independent of the diffusion weighting above $b = 4000$ s/mm^2, as should be the case for intrinsic tissue properties, also supports this as an appropriate b-value threshold for FBI. For our experiments, this picture appears to hold up to at least b-values of 10,000 s/mm^2, although it is expected to eventually breakdown for extremely large b-values when the wavelength of the associated q-vector becomes comparable to axonal radii (Jensen et al., 2016; Veraart et al., 2018b). More practically, on currently available clinical scanners, it is challenging to obtain high quality HARDI data with b-values much beyond 6000 s/mm^2 due to signal noise. Thus, a b-value range of 4000–6000 s/mm^2 can be recommended in most circumstances for FBI at 3 T. But it should be emphasized that all of our results were obtained for healthy, young adults. For young children and adults with severe neuropathology or for fixed brain tissue, it is possible that the optimal range of b-values may differ.

Another important consideration in applying FBI is choosing the number of diffusion-encoding directions. Increasing the number of diffusion-encoding directions improves both the accuracy and precision with which the signal's spherical harmonic expansion coefficients can be computed but at the price of a longer scan time. The original work on FBI employed 256 diffusion-encoding directions with scan times of over 30 min (Jensen et al., 2016), which is prohibitive for many potential applications, especially clinically. Here we find that as few as 64 diffusion-encoding directions are adequate, which is consistent with prior numerical simulations for an FBI-based microstructural modeling method (McKinnon et al., 2018). This allows whole brain FBI datasets to be acquired in less than 5 min when using a multiband acceleration factor of 2. However, 30 diffusion-encoding directions are too few for the reliable estimation of ζ and FAA, as shown in Fig. 6.

The choice of TE is also vital for ensuring sufficient SNR while still adhering to the main underlying FBI assumptions. We find minimal change in the microstructural parameters of FBI and the estimated fODF for TE ranging from 90 to 120 ms at the fixed b-value of 4000 s/mm^2 (Fig. 7 and 17), although some decrease in precision is apparent as the TE is increased (Fig. 8). Due to scanner hardware limitations, we were unable to decrease the TE below 90 ms at the fixed b-value of 4000 s/mm^2

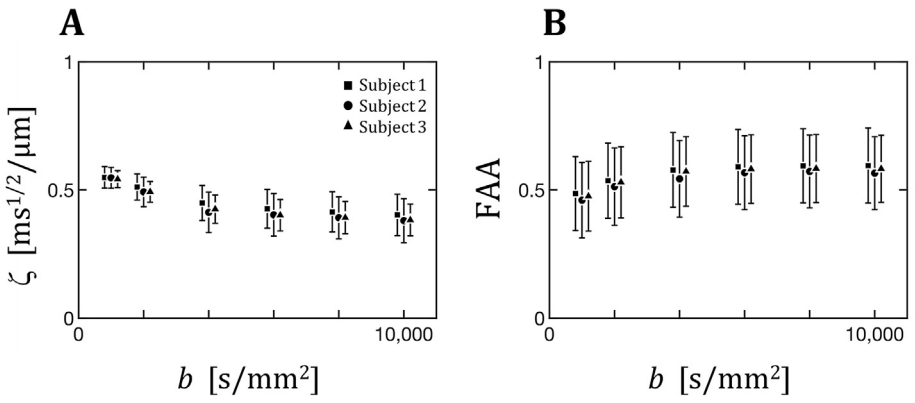

Fig. 4. Mean values for ζ and FAA over all WM voxels from three subjects as functions of b-value. Both parameters are fairly constant for $b \geq 4000$ s/mm^2 suggesting this to be approximately the minimum diffusion weighting needed for reasonable accuracy with FBI. The calculations utilized 128 diffusion-encoding directions. Some subject data points have been slightly displaced in the horizontal direction to improve readability, and the error bars indicate standard deviations.

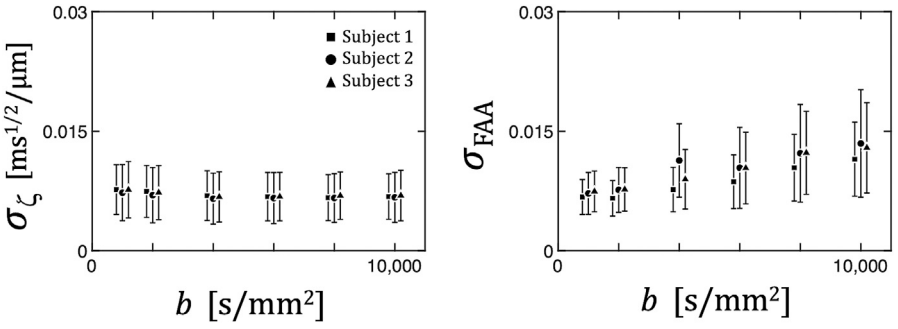

Fig. 5. Voxel-wise standard deviations for ζ and FAA (σ_ζ and σ_{FAA}) averaged over all WM voxels as functions of b-value. These were calculated from numerical simulations based on adding Rician noise to the previously processed HARDI data from three subjects. The voxel-wise standard deviations for ζ are relatively insensitive to the b-value, but they grow noticeably with increasing b-value for FAA. Note that for both parameters their voxel-wise standard deviations are only a few percent of their mean values shown in Fig. 4. Some subject data points have been slightly displaced in the horizontal direction to improve readability, and the error bars reflect the spread over all WM of the voxel-wise standard deviations.

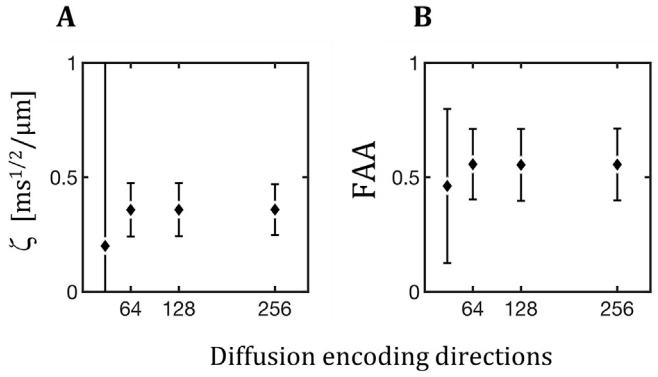

Fig. 6. Mean values for ζ and FAA over all WM voxels from a single subject (Subject 4) as functions of the number of diffusion-encoding directions with $b = 6000$ s/mm^2. The number of diffusion-encoding directions used were 30, 64, 128, and 256. Similar values are found with 64 directions and above indicating that 64 directions are sufficient for estimation of these two microstructural parameters. However, discrepant values are obtained when only 30 directions are used showing this to be inadequate sampling. Error bars signify standard deviations.

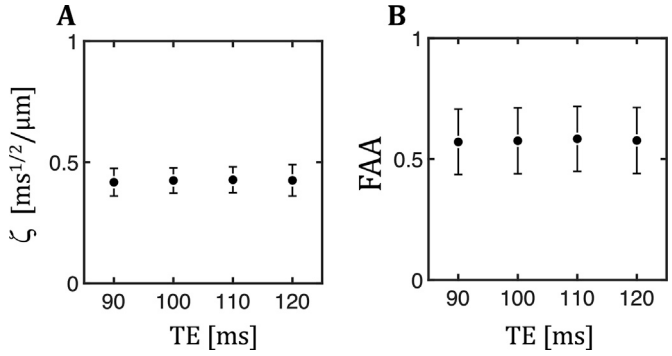

Fig. 7. Mean values for ζ and FAA over all WM voxels from a single subject (Subject 5) as functions of TE with $b = 4000$ s/mm^2 and 128 diffusion-encoding directions. For TE varying between 90 and 120 ms, little change in the parameter values is observed. Error bars signify standard deviations.

tested here.

In the high b-value regime (considered here to be $b \geq 4000$ s/mm^2), the SNR for our experiments ranged from 7 to 14. The effect of noise on the microstructural parameters and estimated fODF of FBI was investigated with numerical simulations by adding Rician noise to the previously processed HARDI data, denoising once more and then running it through the analysis pipeline. This procedure was repeated 100 times for each b-value (Subjects 1–3) and for each TE (Subject 5). From these numerical simulations, we find that the precision of the microstructural parameters to be a few percent (Figs. 5 and 8) and a few degrees for the principal fODF direction (Figs. 15 and 18).

We have considered two different variants of the fODF as calculated with FBI. The first is based on the conventional inverse Funk transform of HARDI data for a specified b-value shell. The second modifies the inverse Funk transform by introducing the function $g_{2l}(bD_0)$, where D_0 is a diffusivity scale that must obey the constraint $D_0 \geq D_a$. As $D_0 \to \infty$, $g_{2l}(bD_0)$ tends to unity, and this generalized inverse Funk transform reduces to the conventional inverse Funk transform. On the other hand, as $D_0 \to D_a$, the accuracy of the FBI estimates of the spherical harmonic expansion coefficients should improve (Jensen et al., 2016). Since the intra-axonal diffusivity D_a would not usually be known in advance, we set D_0 equal to the 37 °C free water diffusivity of 3.0 μm^2/ms, which is presumably an upper bound for D_a. (While it is true that our analysis of the harmonic power for the dMRI signal provides a value for D_a, this

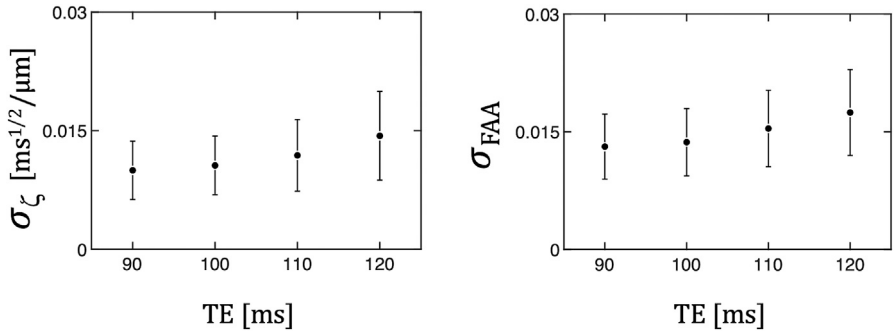

Fig. 8. Voxel-wise standard deviations for ζ and FAA (σ_ζ and σ_{FAA}) averaged over all WM voxels as functions of TE. These were calculated from numerical simulations based on adding Rician noise to the previously processed HARDI data from Subject 5. For both parameters, the voxel-wise standard deviations tend in grow with increasing TE. The error bars reflect the spread over all WM of the voxel-wise standard deviations.

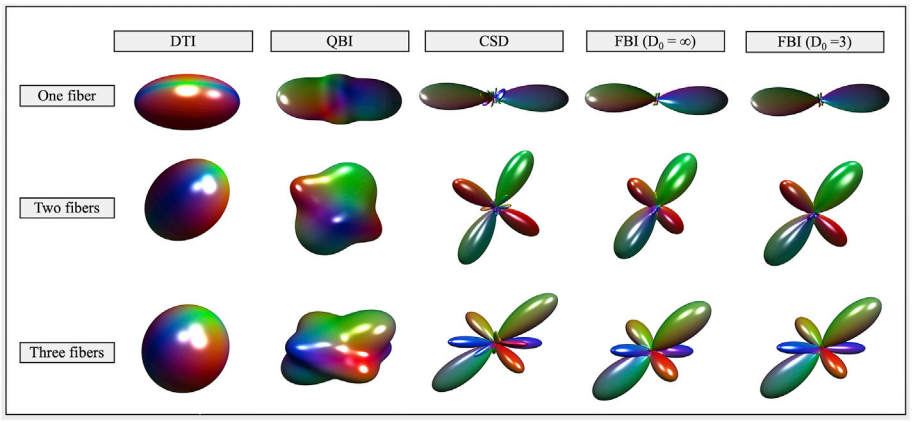

Fig. 9. Diffusion ellipsoids calculated from DTI (b = 1000 s/mm^2), dODFs calculated from QBI (b = 6000 s/mm^2), and fODFs calculated from CSD and FBI (b = 6000 s/mm^2) for voxels with single and crossing fibers. The two FBI fODFs are calculated with $D_0 = \infty$ (uncorrected fODF) and with $D_0 = 3.0$ μm^2/ms (corrected fODF). The QBI dODF improves upon the DTI ellipsoid by resolving the fiber crossings while the fODFs of CSD and FBI are substantially sharper than the dODF. Note also that the corrected fODF is slightly sharper than the uncorrected fODF.

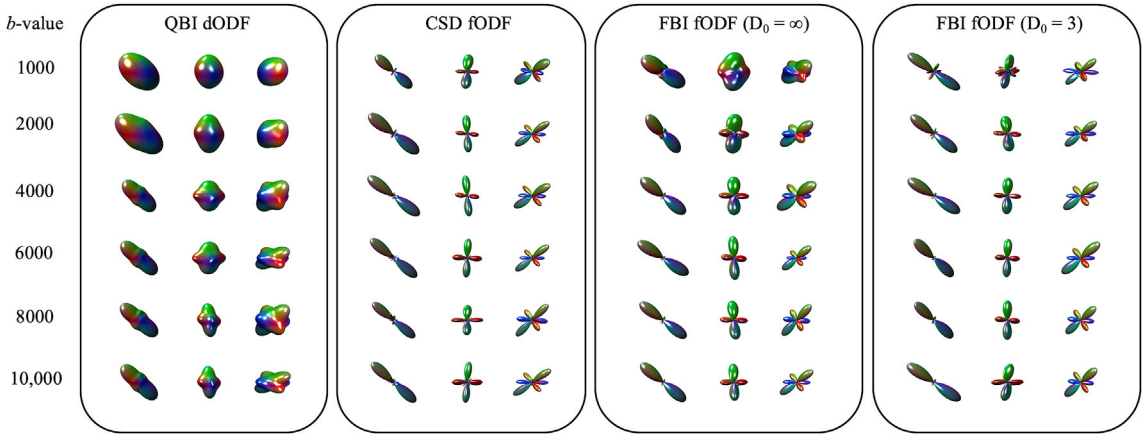

Fig. 10. The estimates across b-values for the QBI dODF, the CSD fODF, and the uncorrected ($D_0 = \infty$) and corrected ($D_0 = 3.0$ μm^2/ms) FBI fODFs. These come from the same three voxels as in Fig. 9 containing single and crossing fibers (but the orientations have been altered for display purposes). As b is increased, notice that the two FBI fODF variants converge to similar shapes by approximately b = 4000 s/mm^2, and there are only minor observable differences for b = 10,000 s/mm^2. The CSD fODFs have sharp features, even for low b-values, and they are similar to the corrected FBI fODFs at b-values of 2000 s/mm^2 and above. The QBI dODF peaks are not conspicuous until roughly b = 4000 s/mm^2 where definite peak directions begin to emerge.

requires multiple b-value shells and is not applicable to the many voxels for which the amplitudes of the $l \geq 4$ harmonics are near or below the noise floor.) We find that the corrected fODF with $D_0 =$ 3.0 μm^2/ms differs only slightly from the uncorrected fODF calculated with the conventional inverse Funk transform for $b \geq$ 4000 s/mm^2. The corrected fODF is slightly sharper (Figs. 9 and 10), but the uncorrected fODF is less sensitive to signal noise and takes on fewer unphysical negative values (Fig. 19). Moreover, Fig. 11 shows that the FAA of the corrected fODF has higher anisotropy and thus sharper features than the uncorrected fODF, although the FAA differences are small for $b \geq$ 6000 s/mm^2. Based on these results, we do not strongly recommend one variant over the other.

The close link between FBI and QBI is most evident from the fact that the dODF of QBI is precisely the double Funk transform of the uncorrected fODF of FBI. As a consequence, the QBI dODF will always be

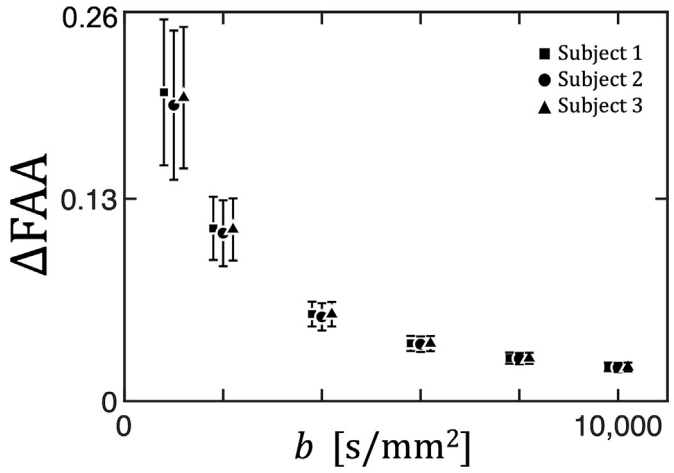

Fig. 11. Mean difference between FAA values for the corrected ($D_0 = 3.0\,\mu m^2/ms$) and uncorrected ($D_0 = \infty$) FBI fODFs as a function of *b*-value for three subjects. Due to sharper features, the FAA for the corrected fODF is always larger than for the uncorrected fODF. The difference between the fODF variants decreases as the *b*-value is increased. Some subject data points have been slightly displaced in the horizontal direction to improve readability, and the error bars indicate standard deviations.

smoother than the FBI fODF, which implies that the axonal fiber bundle orientations are better delineated with FBI leading to more extensive WMFT (Fig. 20). Since the data requirements for QBI and FBI are identical and since they employ similar computational methods, we suggest that FBI be preferred for WM applications. However, an advantage of QBI is that it has a theoretical basis independent of any assumptions regarding tissue microstructure (Tuch, 2004), and so its use may be better justified in WM with severe pathology or in other tissue types (Dierckx et al., 2009).

A variety of alternative dMRI methods for estimating fODFs have been developed (Anderson, 2005; Daducci et al., 2014; Schilling et al., 2018; Tournier et al., 2004, 2007; Wilkins et al., 2015). The distinctive features of the FBI approach are: 1) it is based on a straightforward linear transformation, the inverse Funk transform, and thereby avoids the need for complex numerical fitting; 2) it only employs intra-voxel information without fixing any parameters or other quantities globally (with a minor exception for D_0 with the corrected fODF); 3) it makes only minimal, well-supported assumptions about WM microstructure. For example, the CSD technique requires, in contrast, both numerical regularization and a globally defined response function in order to find the fODF (Tournier et al., 2007). This is not to imply that such alternative methods do not have potential advantages. An advantage of CSD relative to FBI is that it does not assume the *b*-value to be so high that the signal from the extra-axonal space is largely suppressed, which allows CSD to be applied to lower *b*-value datasets than is appropriate for FBI. While CSD fODFs were included here for visual reference, a quantitative investigation that compares FBI fODFs with fODFs generated using other approaches would be a valuable extension of this study.

One application of FBI is the calculation of WMFT. Here FBI simply supplies the fODF, which then can be incorporated into one of many established fiber tracking algorithms (Jeurissen et al., 2019; Lazar, 2010). For deterministic WMFT, it is usually just the directions of the fODF peaks that are employed, with FBI sharing the advantage, relative

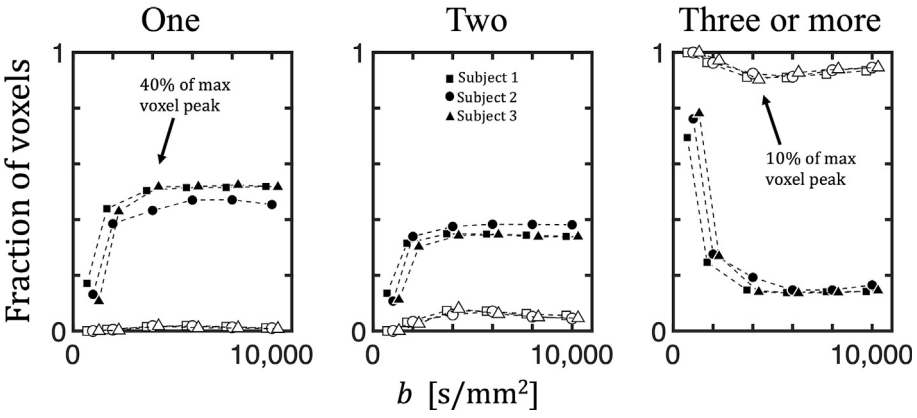

Fig. 12. Fraction of WM voxels from three subjects with one, two, and three or more fODF peak directions as a function of *b*-value. The number of directions in each voxel was determined by using peak threshold factors of 10% or 40% of the maximum peak amplitude. At the 40% threshold, the voxel fractions are nearly constant for $b \geq 4000$ s/mm^2. For lower *b*-values, the voxel fractions deviate substantially, implying that the fODFs are not reconstructed accurately. For the 10% threshold, most of the WM voxels have three or more peak directions, in contrast to the small number with three or more peak directions using the 40% threshold for $b \geq 4000$ s/mm^2.

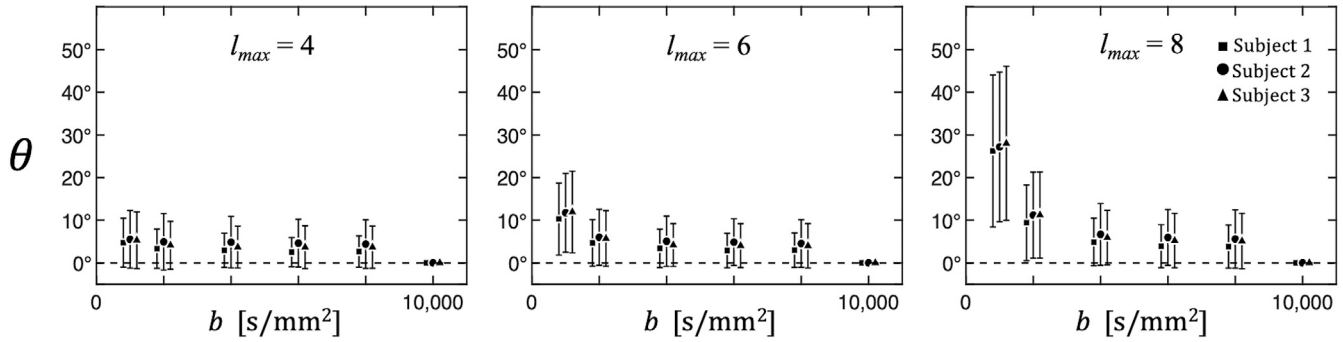

Fig. 13. Mean angular difference (θ) between the principal fODF direction and a reference direction (principal direction at $b = 10,000$ s/mm^2) over all WM voxels from each of three subjects as a function of *b*-value for maximum spherical harmonic degrees of $l_{max} = 4$, 6, and 8. The angular differences are all similar for 4000 s/mm$^2 \leq b \leq$ 8000 s/mm^{2}but increase for smaller b-values, depending on l_{max}. The $l_{max} = 8$ values tend to be larger, which may reflect the greater noise sensitivity of the higher degree harmonics. The data points for $b = 10,000$ s/mm^2 are zero by definition. Some subject data points have been slightly displaced in the horizontal direction to improve readability, and the error bars indicate standard deviations.

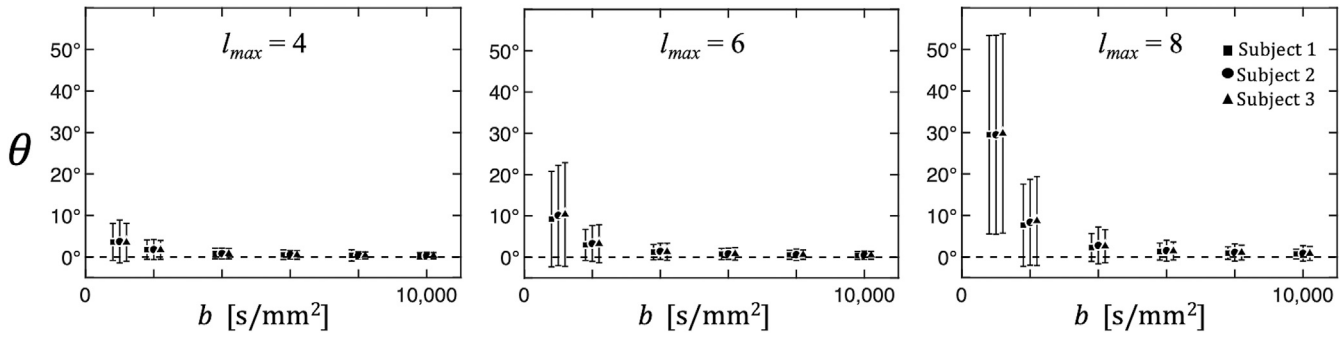

Fig. 14. Mean angular difference (θ) between the principal fODF directions as calculated with $D_0 = 3.0\ \mu m^2/ms$ (corrected fODF) and $D_0 = \infty$ (uncorrected fODF) over all WM voxels from each of three subjects as a function of b-value for maximum spherical harmonic degrees of $l_{max} = 4$, 6, and 8. The angular differences are approximately two degrees or less for $b \geq 4000\ s/mm^2$. This shows that the principal fODF directions are insensitive to the choice of D_0 for $b \geq 4000\ s/mm^2$. Some subject data points have been slightly displaced in the horizontal direction to improve readability, and the error bars indicate standard deviations.

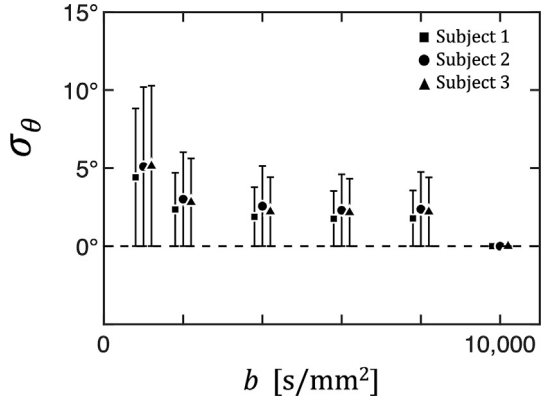

Fig. 15. Voxel-wise standard deviations for angular difference (σ_θ) between the principal fODF direction and a reference direction (principal direction at $b = 10,000\ s/mm^2$) averaged over all WM voxels from each of three subjects (Subjects 1–3) as a function of *b*-value. These were calculated from numerical simulations based on adding Rician noise to the previously processed HARDI data for the three subjects. The voxel-wise standard deviations are all similar for $4000\ s/mm^2 \leq b \leq 8000\ s/mm^2$. The data points for $b = 10,000\ s/mm^2$ are zero by definition. Some subject data points have been slightly displaced in the horizontal direction to improve readability, and the error bars reflect the spread over all WM of the voxel-wise standard deviations.

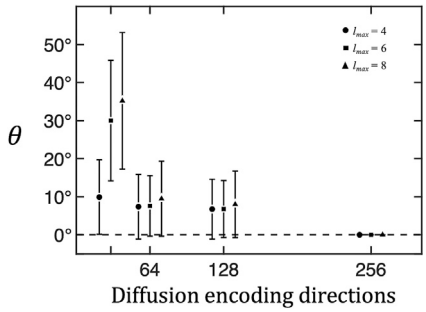

Fig. 16. Angular differences (θ) between the principal fODF direction and a reference direction (principal direction for 256 diffusion-encoding directions) averaged over all WM voxels from a single subject (Subject 4) as a function of the number of diffusion-encoding directions for $l_{max} = 4$, 6 and 8. Similar values are found with 64 and 128 directions, with little dependence on l_{max}, but substantially higher values are obtained when only 30 directions are used with $l_{max} = 6$ or 8. The data points for 256 directions are zero by definition. Error bars signify standard deviations.

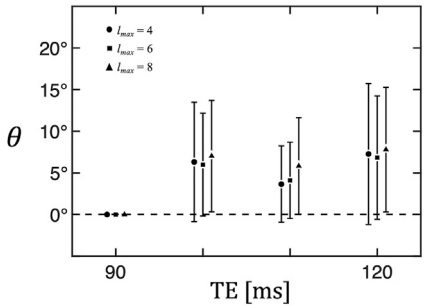

Fig. 17. Angular differences (θ) between the principal fODF direction and a reference direction (principal direction for TE = 90 ms) averaged over all WM voxels from a single subject (Subject 5) as a function of TE for $l_{max} = 4$, 6 and 8. Similar values are found for all echo times other than for TE = 90 ms, which is zero by definition. There is also with little dependence on l_{max}. Error bars signify standard deviations.

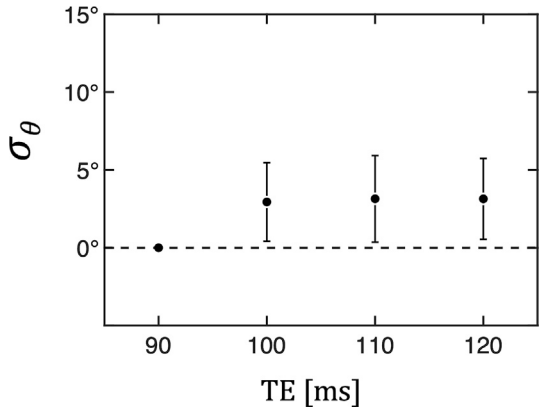

Fig. 18. Voxel-wise standard deviations for angular differences (σ_θ) between the principal fODF direction and a reference direction (principal direction for TE = 90 ms) averaged over all WM voxels from a single subject (Subject 5) as a function of TE. These were calculated from numerical simulations based on adding Rician noise to the subject's previously processed HARDI data. Similar values are found for all echo times other than TE = 90 ms, which is zero by definition. The error bars reflect the spread over all WM of the voxel-wise standard deviations.

to DTI, of most other advanced WMFT techniques in being able to resolve intra-voxel fiber crossings. For probabilistic WMFT, the full fODF could be used to construct a probability distribution of possible directions for each WM voxel. Here we have only given examples of deterministic

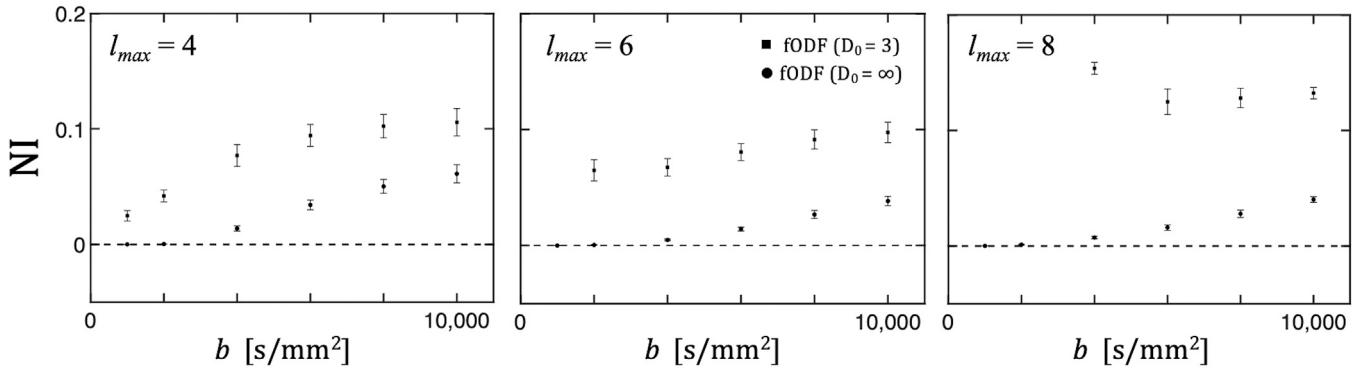

Fig. 19. Average NI versus b-value for three subjects with maximum spherical harmonic degrees of $l_{max} = 4$, 6, and 8. The square data points are for the corrected fODF, while the circular data points are for the uncorrected fODF. A substantially lower NI is found for the uncorrected fODF. In all cases, the NI is small in comparison to one indicating that most fODF values are positive. That the NI is higher for the corrected fODF is likely a consequence of signal noise, the effects of which are amplified as D_0 is decreased. The error bars represent inter-subject standard deviations.

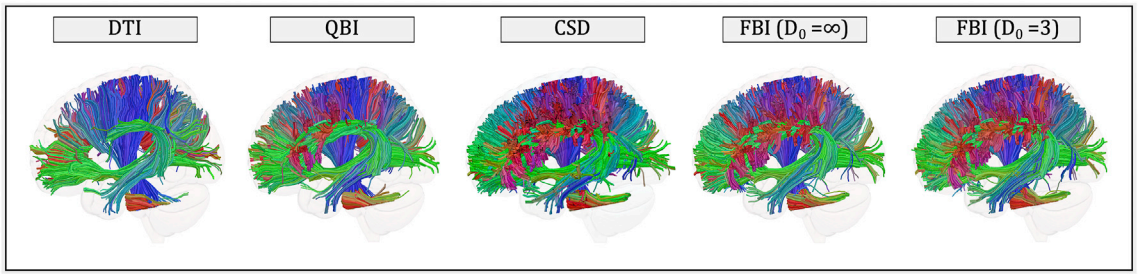

Fig. 20. Whole-brain, deterministic WMFT generated from DTI, QBI, CSD and FBI. Identical seed points, fiber tracking algorithms, and track termination criteria were used in all cases, so that any discrepancies are due solely to differences in the number and directions of the peaks identified by the four methods. FBI-based and CSD-based WMFT produce the most extensive set of fiber tracks, due to their greater sensitivity to fiber crossings. FBI-based WMFT appears similar whether the uncorrected ($D_0 = \infty$) or corrected ($D_0 = 3.0$ μm^2/ms) fODF is used. In contrast, DTI-based and QBI-based WMFT are sparser as is apparent, for example, in the corpus callosum (shown in red) where it crosses the superior longitudinal fasciculus (shown in green).

WMFT based on FBI to demonstrate the feasibility of this; hence, more work remains to be done in this regard.

The fact that extra-axonal water is relatively more mobile than intra-axonal water in directions perpendicular to an axonal fiber bundle has the consequence, as we have discussed, that the spherical harmonic expansion coefficients of HARDI data are dominated, for high b-values, by contributions from intra-axonal water. FBI takes advantage of this to obtain a remarkably simple expression for the fODF as well as for the microstructural parameters ζ and FAA. A notable feature of the FBI fODF and FAA is that they are specific to axons and thus not influenced by the extra-axonal space. This is quite different from most conventional diffusion parameters, such as the MD and FA, which reflect properties of both intra-axonal and extra-axonal water. The axon specificity of the fODF and FAA may be valuable in clarifying the microstructural origin of diffusion changes associated with pathology. For example, cerebral edema would be expected to strongly affect the MD and FA but not the FAA.

Similar considerations apply to partial volume effects due to cerebrospinal fluid (CSF), which can significantly alter both the MD and FA in certain brain regions (Bhagat and Beaulieu, 2004). Because the FBI fODF and FAA are axon-specific, they are immune to CSF contamination. However, CSF may alter the parameter ζ, since it is proportional to the axonal water fraction. More problematic is gray matter contamination, as may be particularly pronounced for subcortical WM within gyri. In this case, the strong diffusion-weighting used with FBI is not necessarily adequate to suppress the gray matter signal, resulting in errors to the estimated FBI parameters. But for most deep WM voxels this should not be an issue.

An outstanding question regarding the interpretation of FBI is whether it includes contributions from intra-axonal water within unmyelinated axons, but there is reason to think that this is not the case. In particular, the direction-averaged signal in gray matter does not obey the $b^{-1/2}$ scaling behavior found in WM (McKinnon et al., 2017), even though gray matter contains many axons (Chklovskii et al., 2002). This could be explained if unmyelinated axons, which predominate in gray matter, have a higher water permeability than myelinated axons so as to invalidate the basic assumption of FBI that water exchange between the intra-axonal and extra-axonal spaces can be neglected on time scales relevant to dMRI. Such a higher water permeability for unmyelinated axons could conceivably be mediated by a greater density of ion channels that co-transport water (Bai et al., 2018; MacAulay and Zeuthen, 2010; Nilsson et al., 2013). Although most axons in WM are myelinated, certain regions, such as the genu of the corpus callosum, also contain a significant number of unmyelinated axons (Aboitiz et al., 1992; LaMantia and Rakic, 1990), which might then impact parameter estimates obtained with FBI.

There is also a possibility of some extra-axonal water within glial processes contributing significantly to the dMRI signal above the b-value scaling regime threshold of 4000 s/mm^2, as should be the case if these processes are well modeled as impermeable cylinders. However, this is difficult to reconcile with the lack of scaling observed in gray matter (McKinnon et al., 2017), which contain an abundance of similar processes, as well as with relaxation time experiments that suggest intra-cellular and extra-cellular water outside of myelinated axons are in rapid exchange (Does and Gore, 2002).

5. Conclusion

In normal WM for b-values exceeding about 4000 s/mm^2, the direction-averaged dMRI signal at 3 T and the signal's harmonic powers

follow closely the predictions of FBI, supporting its validity for this range of diffusion weightings. Moreover, associated microstructural parameters and basic features of FBI fODFs vary little with *b*-value above this 4000 s/mm^2 threshold, as is expected for intrinsic tissue properties. The microstructural parameters and the fODF were found to be robust in the presence of signal noise and had little TE dependence within the range of 90–120 ms. At least 64 diffusion-encoding directions are adequate for FBI, but 30 diffusion-encoding directions are insufficient. A dODF obtained with QBI corresponds precisely to an FBI fODF that has been smoothed by attenuating the higher degree spherical harmonics. As a consequence, FBI is able to generate more comprehensive WMFT than QBI.

Acknowledgments

This work was supported, in part, by National Institutes of Health grants, F31NS108623 (to H. Moss), T32GM008716 (to N. Demore) and T32DC0014435 (to J. Dubno), as well as by a grant from the Litwin Foundation (to J.A. Helpern). We are also grateful for helpful conversations with Andreana Benitez, Leo Bonilha, Rano Chatterjee, and Maria Matheus.

Appendix A. Supplementary data

Supplementary data to this article can be found online at https://doi.org/10.1016/j.neuroimage.2019.07.005.

References

Aboitiz, F., Scheibel, A.B., Fisher, R.S., Zaidel, E., 1992. Fiber composition of the human corpus callosum. Brain Res. 598, 143–153.
Aganj, I., Lenglet, C., Sapiro, G., Yacoub, E., Ugurbil, K., Harel, N., 2010. Reconstruction of the orientation distribution function in single-and multiple-shell q-ball imaging within constant solid angle. Magn. Reson. Med. 64, 554–566.
Anderson, A.W., 2005. Measurement of fiber orientation distributions using high angular resolution diffusion imaging. Magn. Reson. Med. 54, 1194–1206.
Bai, R., Springer Jr., C.S., Plenz, D., Basser, P.J., 2018. Fast, Na(+)/K(+) pump driven, steady- state transcytolemmal water exchange in neuronal tissue: a study of rat brain cortical cultures. Magn. Reson. Med. 79, 3207–3217.
Bailey, T.N.E., M.G, Gover, R., Mason, L.J., 2003. Complex analysis and the Funk transform. J. Korean Math. Soc. 40, 577–593.
Bhagat, Y.A., Beaulieu, C., 2004. Diffusion anisotropy in subcortical white matter and cortical gray matter: changes with aging and the role of CSF-suppression. J. Magn. Reson. Imaging 20, 216–227.
Bush, E.C., Allman, J.M., 2003. The scaling of white matter to gray matter in cerebellum and neocortex. Brain Behav. Evol. 61, 1–5.
Canales-Rodríguez, E.J., Melie-García, L., Iturria-Medina, Y., 2009. Mathematical description of q-space in spherical coordinates: exact q-ball imaging. Magn. Reson. Med. 61, 1350–1367.
Chklovskii, D.B., Schikorski, T., Stevens, C.F., 2002. Wiring optimization in cortical circuits. Neuron 34, 341–347.
Daducci, A., Canales-Rodriguez, E.J., Descoteaux, M., Garyfallidis, E., Gur, Y., Lin, Y.C., Mani, M., Merlet, S., Paquette, M., Ramirez-Manzanares, A., Reisert, M., Reis Rodrigues, P., Sepehrband, F., Caruyer, E., Choupan, J., Deriche, R., Jacob, M., Menegaz, G., Prckovska, V., Rivera, M., Wiaux, Y., Thiran, J.P., 2014. Quantitative comparison of reconstruction methods for intra-voxel fiber recovery from diffusion MRI. IEEE Trans. Med. Imaging 33, 384–399.
Descoteaux, M., Angelino, E., Fitzgibbons, S., Deriche, R., 2007. Regularized, fast, and robust analytical Q-ball imaging. Magn. Reson. Med. 58, 497–510.
Dhital, B., Reisert, M., Kellner, E., Kiselev, V.G., 2019. Intra-axonal diffusivity in brain white matter. Neuroimage 189, 543–550.
Dierckx, H., Benson, A.P., Gilbert, S.H., Ries, M.E., Holden, A.V., Verschelde, H., Bernus, O., 2009. Intravoxel fibre structure of the left ventricular free wall and posterior left-right ventricular insertion site in canine myocardium using Q-Ball imaging. In: Sermesant, M., Ayache, N., Delingette, H. (Eds.), Functional Imaging and Modeling of the Heart. FIMH 2009. Lecture Notes in Computer Science, 5528. Springer, Berlin, Heidelberg, pp. 495–504.
Does, M.D., Gore, J.C., 2002. Compartmental study of T1 and T2 in rat brain and trigeminal nerve in vivo. Magn. Reson. Med. 47, 274–283.
Funk, P., 1913. Über Flächen mit lauter geschlossenen geodätischen Linien. Math. Ann. 74, 278–300.
Funk, P., 1915. Über eine geometrische Anwendung der Abelschen Integralgleichung. Math. Ann. 77, 129–135.
Gelb, A., 1997. The resolution of the Gibbs phenomenon for spherical harmonics. Math. Comput. 66, 699–717.
Glenn, G.R., Helpern, J.A., Tabesh, A., Jensen, J.H., 2015. Optimization of white matter fiber tractography with diffusional kurtosis imaging. NMR Biomed. 28, 1245–1256.
Grebenkov, D.S., 2007. NMR survey of reflected Brownian motion. Rev. Mod. Phys. 79, 1077–1137.
Gudbjartsson, H., Patz, S., 1995. The Rician distribution of noisy MRI data. Magn. Reson. Med. 34, 910–914.
Hess, C.P., Mukherjee, P., Han, E.T., Xu, D., Vigneron, D.B., 2006. Q-ball reconstruction of multimodal fiber orientations using the spherical harmonic basis. Magn. Reson. Med. 56, 104–117.
Holz, M., Heil, S.R., Sacco, A., 2000. Temperature-dependent self-diffusion coefficients of water and six selected molecular liquids for calibration in accurate 1H NMR PFG measurements. Phys. Chem. Chem. Phys. 2, 4740–4742.
Jensen, J.H., Helpern, J.A., 2010. MRI quantification of non-Gaussian water diffusion by kurtosis analysis. NMR Biomed. 23, 698–710.
Jensen, J.H., Helpern, J.A., 2018. Characterizing intra-axonal water diffusion with direction-averaged triple diffusion encoding MRI. NMR Biomed. 31, e3930.
Jensen, J.H., Helpern, J.A., Ramani, A., Lu, H., Kaczynski, K., 2005. Diffusional kurtosis imaging: the quantification of non-Gaussian water diffusion by means of magnetic resonance imaging. Magn. Reson. Med. 53, 1432–1440.
Jensen, J.H., Glenn, G.R., Helpern, J.A., 2016. Fiber ball imaging. Neuroimage 124, 824–833.
Jensen, J.H., McKinnon, E.T., Glenn, G.R., Helpern, J.A., 2017. Evaluating kurtosis-based diffusion MRI tissue models for white matter with fiber ball imaging. NMR Biomed. 30, e3689.
Jeurissen, B., Descoteaux, M., Mori, S., Leemans, A., 2019. Diffusion MRI fiber tractography of the brain. NMR Biomed. e3785. https://doi.org/10.1002/nbm.3785.
Jeurissen, B., Leemans, A., Tournier, J.D., Jones, D.K., Sijbers, J., 2013. Investigating the prevalence of complex fiber configurations in white matter tissue with diffusion magnetic resonance imaging. Hum. Brain Mapp. 34, 2747–2766.
Kaden, E., Kelm, N.D., Carson, R.P., Does, M.D., Alexander, D.C., 2016. Multi-compartment microscopic diffusion imaging. Neuroimage 139, 346–359.
Kellner, E., Dhital, B., Kiselev, V.G., Reisert, M., 2016. Gibbs-ringing artifact removal based on local subvoxel-shifts. Magn. Reson. Med. 76, 1574–1581.
LaMantia, A.S., Rakic, P., 1990. Cytological and quantitative characteristics of four cerebral commissures in the rhesus monkey. J. Comp. Neurol. 291, 520–537.
Lazar, M., 2010. Mapping brain anatomical connectivity using white matter tractography. NMR Biomed. 23, 821–835.
Li, H., Nikam, R., Kandula, V., Chow, H.M., Choudhary, A.K., 2019. Comparison of NODDI and spherical mean signal for measuring intra-neurite volume fraction. Magn. Reson. Imaging 57, 151–155.
MacAulay, N., Zeuthen, T., 2010. Water transport between CNS compartments: contributions of aquaporins and cotransporters. Neuroscience 168, 941–956.
McKinnon, E.T., Jensen, J.H., 2019. Measuring intra-axonal T2 in white matter with direction-averaged diffusion MRI. Magn. Reson. Med. 81, 2985–2994.
McKinnon, E.T., Jensen, J.H., Glenn, G.R., Helpern, J.A., 2017. Dependence on b-value of the direction-averaged diffusion-weighted imaging signal in brain. Magn. Reson. Imaging 36, 121–127.
McKinnon, E.T., Helpern, J.A., Jensen, J.H., 2018. Modeling white matter microstructure with fiber ball imaging. Neuroimage 176, 11–21.
Minkowski, H., 1904. About bodies of constant width. Math. Sbornik 25, 505–508.
Nilsson, M., van Westen, D., Ståhlberg, F., Sundgren, P.C., Lätt, J., 2013. The role of tissue microstructure and water exchange in biophysical modelling of diffusion in white matter. Magn. Reson. Mater. Phys. 26, 345–370.
Novikov, D.S., Kiselev, V.G., Jespersen, S.N., 2018a. On modeling. Magn. Reson. Med. 79, 3172–3193.
Novikov, D.S., Veraart, J., Jelescu, I.O., Fieremans, E., 2018b. Rotationally-invariant mapping of scalar and orientational metrics of neuronal microstructure with diffusion MRI. Neuroimage 174, 518–538.
Quinto, E.T., 2006. An introduction to X-ray tomography and Radon transforms. In: Ólafsson, G., Quinto, E.T. (Eds.), The Radon Transform, Inverse Problems, and Tomography: Proceedings of Symposia in Applied Mathematics, vol. 63, pp. 1–23.
Reese, T.G., Heid, O., Weisskoff, R.M., Wedeen, V.J., 2003. Reduction of eddy-current-induced distortion in diffusion MRI using a twice-refocused spin echo. Magn. Reson. Med. 49, 177–182.
Schilling, K.G., Janve, V., Gao, Y., Stepniewska, I., Landman, B.A., Anderson, A.W., 2018. Histological validation of diffusion MRI fiber orientation distributions and dispersion. Neuroimage 165, 200–221.
Śliwa, W., Soltan, A.M., Freyberg, M.J., 2001. The harmonic power spectrum of the soft X-ray background: I. The data analysis. Astron. Astrophys. 380, 397–408.
Tabesh, A., Jensen, J.H., Ardekani, B.A., Helpern, J.A., 2011. Estimation of tensors and tensor- derived measures in diffusional kurtosis imaging. Magn. Reson. Med. 65, 823–836.
Tournier, J.D., Calamante, F., Gadian, D.G., Connelly, A., 2004. Direct estimation of the fiber orientation density function from diffusion-weighted MRI data using spherical deconvolution. Neuroimage 23, 1176–1185.
Tournier, J.D., Calamante, F., Connelly, A., 2007. Robust determination of the fibre orientation distribution in diffusion MRI: non-negativity constrained super-resolved spherical deconvolution. Neuroimage 35, 1459–1472.
Tournier, J.D., Mori, S., Leemans, A., 2011. Diffusion tensor imaging and beyond. Magn. Reson. Med. 65, 1532–1556.
Tristán-Vega, A., Westin, C.F., Aja-Fernández, S., 2009. Estimation of fiber orientation probability density functions in high angular resolution diffusion imaging. Neuroimage 47, 638–650.
Tuch, D.S., 2004. Q-ball imaging. Magn. Reson. Med. 52, 1358–1372.
Veraart, J., Fieremans, E., Rudrapatna, U., Jones, D.K., Novikov, D.S., 2018b. Breaking the power law scaling of the dMRI signal on the Connectom scanner reveals its sensitivity to axon diameters. Proc. Int. Soc. Magn. Reson. Med. 252. Paris, France.

Veraart, J., Novikov, D.S., Christiaens, D., Ades-Aron, B., Sijbers, J., Fieremans, E., 2016. Denoising of diffusion MRI using random matrix theory. Neuroimage 142, 394–406.
Veraart, J., Fieremans, E., Novikov, D.S., 2019. On the scaling behavior of water diffusion in human brain white matter. Neuroimage 185, 379–387.
Veraart, J., Novikov, D.S., Fieremans, E., 2018a. TE dependent Diffusion Imaging (TEdDI) distinguishes between compartmental T2 relaxation times. Neuroimage 182, 360–369.
Wilkins, B., Lee, N., Gajawelli, N., Law, M., Leporé, N., 2015. Fiber estimation and tractography in diffusion MRI: development of simulated brain images and comparison of multi-fiber analysis methods at clinical b-values. Neuroimage 109, 341–356.
Yang, A.W., Jensen, J.H., Hu, C.C., Tabesh, A., Falangola, M.F., Helpern, J.A., 2013. Effect of cerebral spinal fluid suppression for diffusional kurtosis imaging. J. Magn. Reson. Imaging 37, 365–371.